arXiv:1401.8198v3 [cond-mat.str-el] 12 Oct 2015

Phase diagram of the Hubbard model on the anisotropic triangular lattice

Manuel Laubach,[1] Ronny Thomale,[1] Christian Platt,[2,1] Werner Hanke,[1] and Gang Li[1]

[1] *Institut für Theoretische Physik und Astrophysik, Universität Würzburg, 97074 Würzburg, Germany*
[2] *Department of Physics, Stanford University, Stanford, California 94305, USA*

(Dated: October 13, 2015)

We investigate the Hubbard model on the anisotropic triangular lattice as a suggested effective description of the Mott phase in various triangular organic compounds. Employing the variational cluster approximation and the ladder dual-fermion approach as complementary methods to adequately treat the zero-temperature and the finite-temperature domains, we obtain a consistent picture of the phase diagram as a function of anisotropy and interaction strength. The metal-insulator transition substantially depends on the anisotropy, and so does the nature of magnetism and the emergence of a nonmagnetic insulating phase. We further find that geometric anisotropy significantly influences the thermodynamics of the system. For increased frustration induced by anisotropy, the entropy of the system increases with interaction strength, opening the possibility of adiabatically cooling a frustrated system by an enhancement of electronic correlations.

PACS numbers: 71.30.+h, 71.10.Fd

I. INTRODUCTION

Single crystals of organic charge-transfer salts have recently received substantial interest, and fascinating phenomena such as several emergent many-body phases have been observed. κ-(BEDT-TTF)$_2$Cu[N(CN)$_2$]Cl and κ-(BEDT-TTF)$_2$Cu$_2$(CN)$_3$ are two prototypical examples of such organics: As far as similarities are concerned, the Fermi liquid, Mott insulator behavior, and the crossover between the two phases are similarly detected in both materials[1,2]. The metal-insulator transition is found to be associated with unusual critical exponents which, face value, do not fall into any established universality class[3]. The main difference between these compounds, however, which sparks even more substantial interest, shows up in their magnetic behavior. κ-(BEDT-TTF)$_2$Cu[N(CN)$_2$]Cl displays long-range magnetic order at low temperatures, which is in sharp contrast to the strongly magnetically frustrated behavior of κ-(BEDT-TTF)$_2$Cu$_2$(CN)$_3$. The bulk spin susceptibility[4] of κ-(BEDT-TTF)$_2$Cu$_2$(CN)$_3$ reflects this strong frustration, as it displays no indication of long-range antiferromagnetic order at temperatures significantly lower than the magnetic exchange scale, as inferred from the Heisenberg coupling estimated from high-temperature series expansions[5]. Together, these findings highlight the similarity of the two compounds in the charge sector, and also the clear difference regarding the spin degrees of freedom, which also manifests itself in the effective-field-theory description of the problem[6–9]. Separating charge from spin paves the way for the investigation of effective spinon theories in the Mott insulating phase, with or without gapless spinon modes yielding a potentially unstable spinon Fermi surface[10].

Such effective field theories, however, are not stringently specified and can take on different forms. For example, the low-T thermal conductivity is found to be contributed by the spin-1/2 spinons in a theory of a U(1) gauge field coupled to a spinon Fermi surface[6], but is associated with visons in a $\mathcal{Z}_2$ theory[7]. A puzzling situation similar to that in theory likewise exists on the experimental side. There, the interpretation of the given evidence is far from settled, as specific-heat[11] and thermal-conductivity[12] experiments may yield different conclusions on the nature of the fermionic excitations in κ-(BEDT-TTF)$_2$Cu$_2$(CN)$_3$. On top of all these complications, even if we assume a spin liquid state in the latter compound, it is still debated whether this state would be fully gaped or not[13,14].

What are the microscopic parameters whose variations impose such a diversity of exotic many-body phenomena in the organic compounds? While the interaction strength is probably rather comparable in all these compounds, a clear difference that catches the eye lies in the anisotropy strength inherently determined by the underlying crystal structure and chemical components. The anisotropy strength can be obtained from *ab initio* calculations[15–17]. Assuming the Hubbard model on a triangular lattice is the correct model to describe the interplay of geometric frustration with electronic correlations, it is a natural further step of complexity to consider the lattice anisotropy.

In this paper, we study the Hubbard model on the triangular lattice with varying anisotropy strengths, devising methods to treat both the zero- and finite-temperature regime. The Hamiltoinan is given by

$$\hat{H} = -\sum_{<ij>,\sigma} t_{ij} c^\dagger_{i\sigma} c_{j\sigma} - \mu \sum_{i\sigma} c^\dagger_{i\sigma} c_{i\sigma} + U \sum_i n_{i\uparrow} n_{i\downarrow}, \quad (1)$$

with $\langle ij \rangle$ denoting nearest neighbor bonds, $t_{ij} = t'$ for the horizontal hopping, and $t_{ij} = t$ for the diagonal hopping as shown in Fig. 1. Varying the anisotropy t'/t from the limiting values 0 to 1, we effectively change the lattice geometry from square to triangular type. Unless stated otherwise in the paper, we choose the phrasing of small and large anisotropy according to the value of t'/t. The most interesting regime for the organic compounds is located around the isotropic triangular limit

$t'/t = 1$, where only small variations can yield crucially different scenarios. It is instructive to see how the phase diagram evolves from the square limit towards the triangular limit, which is why we analyze the complete domain $0 \leq t'/t \leq 1.1$. For $t'/t > 1.1$, the system quickly evolves towards an effectively one-dimensional scenario of weakly coupled chains, quickly rejecting magnetic order[18]. This is neither a relevant regime for the organic compounds we focus on, nor particularly suited for the methods employed in this work, which is why the regime $t'/t > 1.1$ will not be further addressed.

This paper is organized as follows. Section II briefly introduces the methodology of the variational cluster approximation (VCA) and the ladder dual-fermion approach (LDFA). For the VCA, we elaborate on several recent methodological refinements to enhance its quantitative accuracy such as treating the hopping as a variational parameter and avoiding artificial broadening to obtain the exact poles of the single-particle Green's function. The zero- and finite-temperature phase diagrams are obtained by VCA and LDFA, respectively, providing a complementary and consistent perspective of the Hubbard model on the anisotropic triangular lattice. Our results are discussed in Sec. III. As a function of the anisotropy parameter from the square to the triangular limit, we find a magnetic phase transition from Néel-antiferromagnetic (AFM) to 120°-AFM order along with a growing metallic regime for weaker Hubbard U. Furthermore, already close to the triangular limit, the onset of a nonmagnetic insulating regime is found, which is the candidate domain for possible spin-liquid states, where the charge degree is frozen without spin ordering. The LDFA additionally offers the possibility of addressing questions of thermodynamics in the Hubbard model. In particular, we find an indication of adiabatic cooling caused by the change of frustration as a function of interaction strength, which might be observed in highly tunable scenarios such as triangular optical lattices loaded with ultra-cold fermionic isotopes. In Sec. IV, we conclude that our analysis sets the initial stage for further investigations of the many-body phases in the Hubbard model on the anisotropic triangular lattice, for which we can identify the promising non-magnetic insulating regime. Whatever unconventional phases may be found in this regime, and whichever effective theories best describe them, the lattice anisotropy is likely to be a crucial microscopic parameter.

II. METHODOLOGY

In this section, we briefly review the methods we employ in this paper, namely, the VCA and the LDFA. These two methods will be subsequently applied for zero and finite temperature, respectively, focusing on the quantum phase diagram and certain thermodynamic properties.

A. $T = 0$: Variational cluster approach

The VCA[19] is based on the self-energy-functional theory (SFT)[20,21], which provides an efficient numerical technique for studying strongly correlated systems, especially in the presence of different competing orders. VCA simplifies the lattice problem, as defined in Eq. (1), to an exactly solvable problem defined in a reference system consisting of decoupled finite-size clusters. The thermodynamic limit is recovered by reintroducing the intercluster hopping to the decoupled cluster via a nonperturbative variational scheme based on SFT. The VCA has been successfully applied to many interesting problems, including the high-T_c cuprates[22–26] and topological insulators[27–29].

In particular, the VCA has already been employed to analyze the Hubbard model on the anisotropic triangular lattice by Sahebsara and Sénéchal 30. It is a method that is particularly suitable for such a study, as the anisotropy induces several phase transitions in the geometrically frustrated system which can be conveniently described within VCA. In Ref. 30, however, the specifications chosen within the VCA, such as the choice of the finite-size cluster, were inadequate to correctly resolve a significant range of the phase diagram. In the following, we will present our VCA in an independent and self-contained fashion. The most important refinements we employ for the VCA to obtain an accurate phase diagram, as well as a detailed comparison to Ref. 30, are explicated in the Appendix.

In the SFT, the grand potential of a system is defined by $H = H_0(\mathbf{t}) + H_1(\mathbf{U})$ and written as a functional of the self-energy Σ:

$$\Omega[\Sigma] = F[\Sigma] + \mathrm{Tr}\ln\left(G_0^{-1} - \Sigma\right)^{-1}, \tag{2}$$

where $F[\Sigma]$ is the Legendre transform of the Luttinger-Ward functional and $G_0 = (\omega + \mu - \mathbf{t})^{-1}$ is the non-interacting Green's function. It can be shown that the functional $\Omega[\Sigma]$ is stationary at the physical self-energy, i.e., $\delta\Omega[\Sigma_{\mathrm{phys}}] = 0$[20]. As the Luttinger-Ward functional is universal, it has the same interaction dependence for systems with any set of single-particle operators $\mathbf{t}'$ as long as the interaction $\mathbf{U}$ remains unchanged. Note that the functional $\Omega[\Sigma]$ itself is not approximated by any means; we restrict, however, the "parameter" space of possible self-energies to the self-energies of the reference system. Thus, the stationary points are obtained from the self-energy $\Sigma' = \Sigma[\mathbf{t}']$ of a system defined by $H' = H_0(\mathbf{t}') + H_1(\mathbf{U})$, which we call the reference system. After defining $V = \mathbf{t} - \mathbf{t}'$, we are able to conveniently define the VCA Green's function,

$$G_{\mathrm{VCA}}^{-1} = G'^{-1} - V\ . \tag{3}$$

The VCA grand potential is

$$\Omega[\Sigma'] = \Omega' + \mathrm{Tr}\ln\left(G_0^{-1} - \Sigma'\right)^{-1} - \mathrm{Tr}\ln(G'), \tag{4}$$

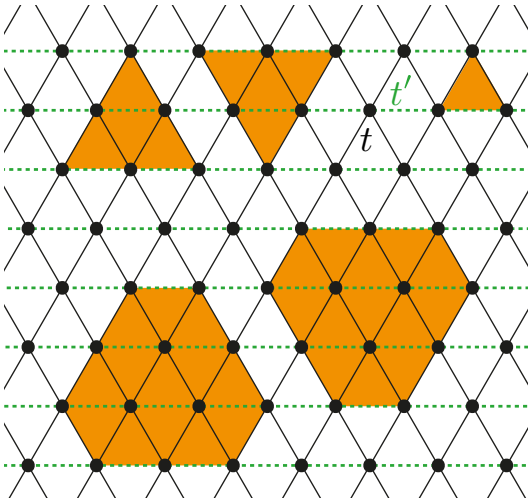

FIG. 1. Anisotropic triangular lattice with diagonal hoppings t(black) and vertical hopping t'(green). The reference clusters are shown for $L_c = 3$, $L_c = 6$, and $L_c = 12$, where the larger clusters are mirrored to recover the lattice geometry. Hoppings between the cluster and its mirror cluster are indicated by the dotted links.

with Ω', Σ', and G' denoting the grand potential, the self-energy, and the single-particle Green's function of the reference system, respectively. The reference system is chosen such that it can be solved exactly; that is, Ω', Σ', and G' should be readily obtained numerically. We choose the reference system as a set of decoupled clusters and solve them with open boundary conditions via exact diagonalization. In this sense, the short-range correlations within the reference system are fully taken into account in the VCA. The correlation beyond the reference system size will be treated in a mean-field fashion via the variational scheme.

The choice of the reference system, *i.e.*, the cluster shape and size, has to respect the fact that tuning the anisotropy from 0 to 1 effectively modifies the system geometry from square to triangular. Thus, a reference system is needed which incorporates both the Néel and spiral orders in the VCA in a commensurate fashion in order not to bias the variational procedure (see also App. A 3). In this paper, two reference systems are explored with cluster sizes of $L_c = 6$ and $L_c = 12$. They are mirrored in our calculation to recover the lattice translation symmetry with a supercluster[31]. The Green's function of this supercluster G' consists of the cluster and mirrored cluster given as,

$$G'^{-1} = \begin{pmatrix} G_1'^{-1} & 0 \\ 0 & G_2'^{-1} \end{pmatrix} + \begin{pmatrix} 0 & t_{21} \\ t_{12} & 0 \end{pmatrix}, \qquad (5)$$

where G_1' is the reference-cluster Green's function and G_2' is the Green's function of the mirrored cluster, which is a simple transformation of G_1' (in the simplest case, it is just a copy of G_1'). The reference and the mirrored clusters are connected through the single-particle hopping t_{12}, as indicated by the dotted links in Fig. 1.

B. Finite-T: Ladder dual-fermion approach

For the finite-temperature study, we employ the dual-fermion approach[32,33], considering only the two-particle vertex and ladder-type diagrams for the self-energy. The dual-fermion approach decouples a correlated lattice defined in Eq. (1) into a group of impurities which couple to each other through an effective interaction mediated by auxiliary dual fermions. The local problem can be well described within the dynamical mean-field theory (DMFT)[34]. The perturbation expansion over the effective interaction of the dual-fermion variables can systematically generate non-local corrections to the DMFT. The basic idea of the dual-fermion approach is schematically shown in Fig. 2, where the lattice problem defined in Fig. 2(a) is decoupled into an impurity problem as in DMFT [Fig. 2(b)]. The difference between the lattice and the decoupled impurity problem is treated perturbatively in the dual-fermion approach [Fig. 2(c)].

Let Fig. 2(a) denote the Hubbard model on a square lattice, where the yellow spheroids represent sites on the lattice. The bond connecting two yellow spheroids represents the hopping between these two sites. When two electrons with different spins stay on the same site, local Hubbard U acts upon them. In the DMFT approximation [Fig. 2(b)], the bonds between different sites are effectively removed, in the sense that each site becomes an impurity coupled to a dynamical bath $\Delta(\omega)$. In Fig. 2(b), $\Delta(\omega)$ is shown as a purple sphere around each site. $t_{ij} - \Delta(\omega)$ associated with the blue bonds in Fig. 2(c) represents the difference between the lattice model in Fig. 2(a) and its DMFT approximation

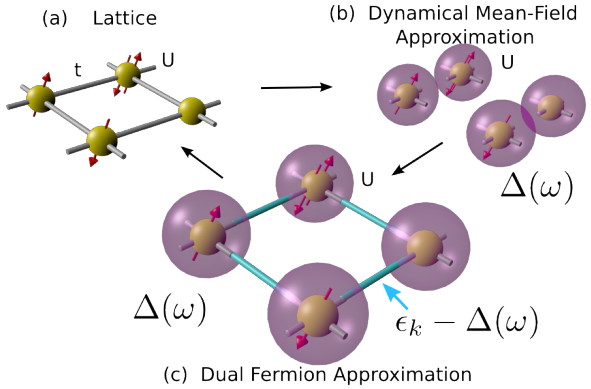

FIG. 2. As a non-local extension of the DMFT, the dual-fermion method perturbatively expands the difference of the single-particle hopping and the DMFT hybridization function, *i.e.*, $\epsilon_k - \Delta(i\omega_n)$, which generates systematic nonlocal corrections to the DMFT solution. Ideally, with all the expansion terms taken into account, the lattice problem defined in (a) can be exactly solved by the dual-fermion method.

in Fig. 2(b). The dual-fermion method then performs a perturbative expansion in terms of this difference, and as such restores momentum dependence starting from the DMFT limit.

Let us formulate the above idea by starting with the lattice action corresponding to the Hamiltonian in Eq. (1):

$$S[c,c^*] = \sum_i S^i_{loc}[c,c^*] + \sum_{n,k,\sigma} [\epsilon_k - \Delta(i\omega_n)] c^*_{k\sigma} c_{k\sigma}. \quad (6)$$

$S^i_{loc}[c,c^*] = -\sum_{n,\sigma} c^\dagger_{k\sigma}(i\omega_n)[i\omega_n + \mu - \Delta(i\omega_n)]c_{k\sigma}(i\omega_n) + U\int n_{i\uparrow}(\tau)n_{i\downarrow}(\tau)d\tau$ is the action of an impurity coupled to a continuum bath. The dynamics of the bath is described by the hybridization function $\Delta(i\omega_n)$. The second sum in Eq. (6) is the term that is treated perturbatively.

If the local action S_{loc} is already a good description of the original system, the second term on the right-hand-side of Eq. (6) will effectively be a small parameter. An expansion in this small term, *i.e.* $\epsilon_k - \Delta(i\omega_n)$, generates further corrections to $S^i_{\rm loc}$ and can be calculated order by order. A convenient way for such an expansion is to rewrite the second term on the right-hand-side of Eq. (6) with a dual variable f, f^* through Gaussian integration. After integrating out the c variables, the original lattice problem described in Eq. (6) now can be equally written as an action that depends on only the f variables:

$$S[f,f^*] = -\sum_{n,k} \ln[\Delta(i\omega_n) - \epsilon_k] - \sum_i \ln \mathcal{Z}^i_{loc} + \sum_i V_i[f^*,f] + \sum_{n,k,\sigma} \left\{[\Delta(i\omega_n) - \epsilon_k]^{-1} + g(i\omega_n)\right\} f^*_{\omega k\sigma} f_{\omega k\sigma}\,. \quad (7)$$

The interaction between the f variables, *i.e.*, V_i in Eq. (7), is the reducible multiparticle vertex of the c variables, which can also be obtained by solving $S^i_{\rm loc}$ with an appropriate impurity solver, such as the continuous-time quantum Monte Carlo method[35].

Equations (6) and (7) are two equivalent ways to describe the same problem, as no approximation is introduced in the transformation. Thus, the lattice Green's function $G_k(i\omega_n)$ can be equally constructed from this new action:

$$G_k(i\omega_n) = [\Delta(i\omega_n) - \epsilon_k]^{-2} g^d_k(i\omega_n) + [\Delta(i\omega_n) - \epsilon_k]^{-1}\,, \quad (8)$$

where $g^d_k(i\omega_n)$ is given as

$$g^d_k(i\omega_n) = [g^{-1}(i\omega_n) + \Delta(i\omega_n) - \epsilon_k - \Sigma^d_k(i\omega_n)]^{-1}\,. \quad (9)$$

It becomes transparent that the problem of solving an interacting many-body problem defined in Eq. (1) is equivalent to solving an Anderson impurity problem, *i.e.*, self-consistently determining $g(i\omega_n)$ and $\Delta(i\omega_n)$, and additionally calculating $\Sigma^d_k(i\omega_n)$ from the perturbation expansion of $V_i[f^*,f]$ in Eq. (7). In the following calculation, we will impose the approximation to consider ladder-type diagrams of $\Sigma^d_k(i\omega_n)$ up to infinite order which contain only the two-particle vertex[33] in the particle-hole channel. With such a simplification employed, the dual-fermion approach is now denoted as LDFA in the following. The LDFA approximation[33], and even the stronger approximation of considering only selective self-energy diagrams from the two-particle vertex[36] have proven fairly accurate in studying strongly correlated electron systems.

Equation (8) sets up an exact relation for the single-particle Green's function of the original c variables and the dual f variables. Similar exact relations can also be found for higher-order correlators. For example, for the spin susceptibility, which is employed to identify different magnetic phases in this work, we have

$$\chi_Q(k,k') = \chi^0_Q(k,k') + h_k h_{k+Q} \tilde{\chi}^d_Q(k,k') h_{k'} h_{k'+Q}\,. \quad (10)$$

Here, $h_k = [\Delta(i\omega_n) - \epsilon_k]^{-1}$ and $\tilde{\chi}^d_Q(k,k') = \chi^d_Q(k,k') - \chi^{d,0}_Q(k,k')$ stands for the reducible vertex of the dual variables. The high momentum resolution of the spin susceptibility calculated from the dual-fermion approach is very hard to achieve in other approaches. In turn, this resolution is vital to studying the spin structure at different anisotropy strengths, as the magnetic order changes from Néel-type [with magnetic wave vector $Q = (\pi,\pi)$] to a 120°-type [with $Q = (2\pi/3, 2\pi/3)$].

III. RESULTS

A. VCA

Figure 3 summarizes the zero-temperature phase diagram as a function of anisotropy and interaction strength as obtained by our VCA calculations. As stated before, the geometrical frustration is parametrized by the size ratio t'/t of the horizontal and diagonal hoppings in Fig. 1. In the strong correlation limit, Eq. (1) is equivalent to the Heisenberg model, and the system develops the Néel-AFM state at $t'/t = 0$[37] and the 120°-AFM state at $t'/t = 1$[38–40]. Varying the anisotropy strength, *i.e.*, changing the value of t'/t, we observe a transition between these two magnetically ordered states. The Néel-AFM state is surprisingly stable against geometric frustration, which, among other methods, has also been found in more sophisticated functional renormalization group studies[18]: Within the VCA, t'/t has to

be larger than 0.89 in order to destroy the collinear antiferromagnetic order to establish the 120°-AFM state. In contrast, in the weak-coupling limit, the geometric frustration plays a much more significant role already for small t'/t, as it stabilizes the metallic phase in the entire range of $t'/t > 0$ for sufficiently small U/t. (On the square lattice and with nearest-neighbor hopping, due to the Fermi surface nesting, the ground state of the system is Néel-ordered already for infinitesimal Hubbard U. The small offset found in Fig. 3 is a minor finite-size artefact in the VCA.) With the increase of t'/t, the metallic state is stabilized and extends up to larger values of U/t. For small t'/t, the metal-insulator transition (MIT) coincides with the development of antiferromagnetic order.

With larger anisotropy, the MIT as a function of coupling strength acquires a different character. In Fig. 3, we observe a transition from a metallic "phase" to a nonmagnetic insulating (NMI) phase. For approximately $5.2 < U/t < 9$, the system opens up a charge gap without developing long-range magnetic order when $t'/t > 0.7$ (see Fig. 3 for the precise boundaries of the metal-NMI and NMI-magnetic transition). The NMI phase is the natural regime where one or several kinds of quantum spin-liquid (QSL) phases might be located. Strong geometric frustration combined with charge fluctuations suppresses the magnetic ordering in this coupling region. Note that since our numerical methods are adjusted to the computation of single-particle quantities, it is impossible for further analyze the specific properties of the NMI phase, which is indispensable to making concrete predictions for the expected spin-liquid states.

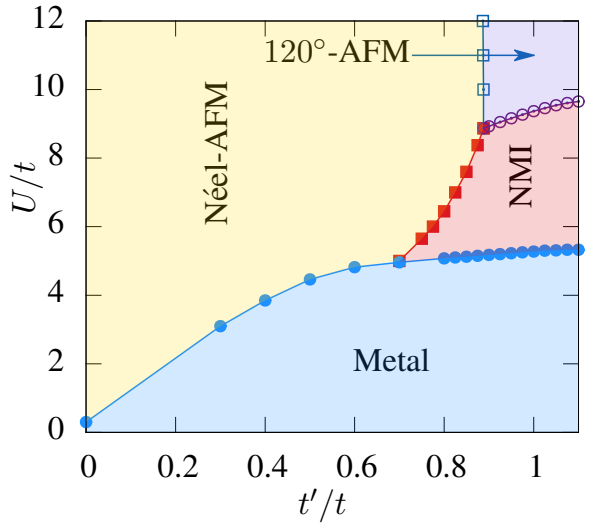

FIG. 3. Zero-temperature VCA phase diagram as a function of anisotropy t'/t and interaction strength U/t. Changing t'/t from 0 to 1 interpolates the system geometry from square to triangular type. Four regimes are identified: paramagnetic metal, Néel-AFM insulator, 120°-AFM insulator, and nonmagnetic insulator (NMI). The phase diagram is based on calculations on a $L_c = 6$ cluster without hopping variation.

The appearance of the NMI phase in the intermediate-coupling region qualitatively agrees with other theoretical investigations[30,31,41–48]. In these works and the present study, the emergence of the NMI phase is consistently shown to be due to the competition between electronic correlation and geometric frustration. However, the size of the NMI phase differs. For VCA, this is partially due to the fact that the lower bound of the NMI phase slightly depends on the cluster size. The metal to NMI phase transition occurs at $U/t = 5.4$ for $L_c = 3$, $U/t = 5.25$ for $L_c = 6$, and $U/t = 6.3$ for $L_c = 12$. As electrons gain more mobility in a larger cluster, the kinetic energy of the ground state will become lower in this case.

Recently, we realized that for hexagonal lattices in particular, this mobility enhancement can be efficiently simulated by introducing another variation parameter, *i.e.*, t, to the VCA procedure[28], (see also Sec. A 1). Hopping t describes the itinerancy of a single electron. The variation of t thus allows us to minimize the kinetic energy, which largely recovers the same physics in a small cluster that would emerge in a larger cluster. In contrast, the upper bound of the NMI phase, *i.e.* the NMI to 120°-AFM phase transition boundary, is determined by the collective behavior of all electrons in the system, and thus is less affected by the variation of single-electron hopping. As a result, we find that, by varying t, the lower bound of the NMI phase becomes $U/t = 7.5$ for the isotropic triangular lattice with $L_c = 6$, while the upper bound $U/t = 9.4$ is unchanged. This is affirmed by calculations on a larger cluster $L_c = 12$, where we find the MIT at $U/t = 7.2$.

In our VCA calculations, the MIT boundary is determined by the opening of the single-particle gap Δ_{sp}. It is directly obtained from the poles of the Green's function with nonzero weight. As such, no broadening of the spectral function and further extrapolation are employed; see Sec. A 2 for more technical details. This allows us to accurately determine the charge gap size from the energy difference between the top of the valence band and the bottom of the conduction band. We find, as displayed

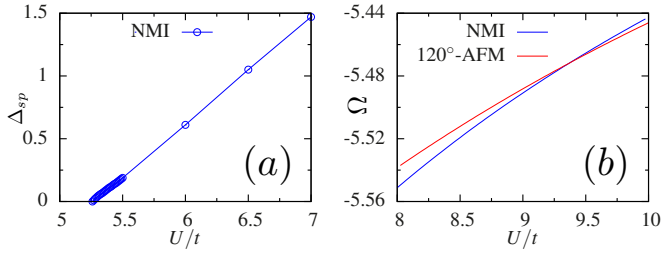

FIG. 4. (a) Single-particle gap as a function of the interaction strength. The opening of the gap marks the phase boundary of the metal and is the lower bound of the NMI phase. (b) The grand potential of the 120°-AFM and the NMI phases as a function of different interactions for $t'/t = 1.0$. The crossing of the grand potential of different phases marks the transition and indicates its first-order nature.

in Fig. 4(a), that the charge gap Δ_{sp} opens at $U = 5.25$ for $t'/t = 1$, indicating a MIT at $U_c = 5.25$. In addition, we also determined the boundary between different magnetic phases as well as the nature of the phase transitions from the comparison of the VCA grand potential for different phases in Fig. 4(b). Around a transition, the preferred phase possesses the lower grand-potential energy, and the transition is characterized by the crossing of the grand-potential energy of different phases. In Fig. 4(b), we show an example of the 120°-AFM to NMI transition for $t'/t = 1.0$. The two VCA grand-potentials cross at $U/t = 9.4$, which indicates that this transition is of first order. (If the two grand potentials smoothly change from one to another without any crossing, the transition is of second order or higher.)

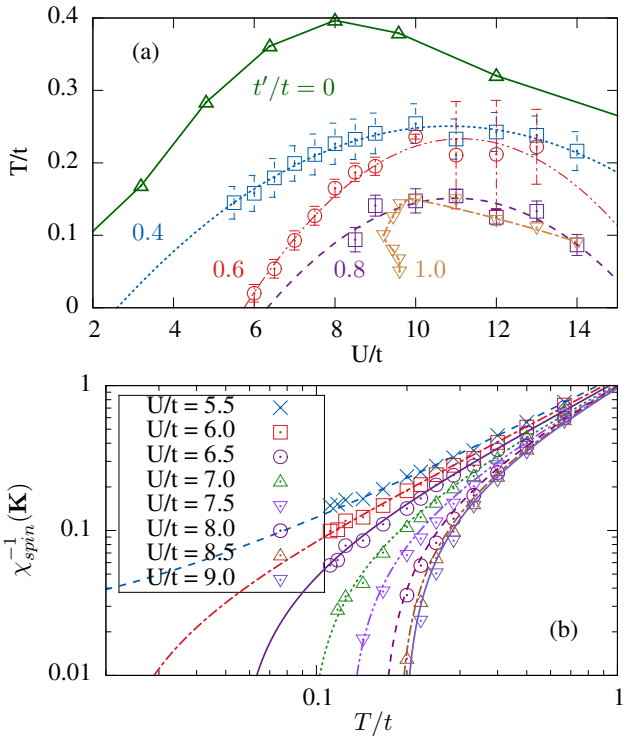

FIG. 5. (a) Néel temperatures as a function of interaction U/t for five different anisotropy strengths (t'/t). The maximum Néel temperature appears to shift to higher U/t values as a function of anisotropy. The error bars represent the uncertainty of the numerical extrapolation. The $t'/t = 1.0$ curve is a replot of the result from Ref. 49. (b) Example for the determination of the Néel temperature via the extrapolation of the inverse spin susceptibility for $t'/t = 0.6$.

B. LDFA

The stabilization of the metallic state due to geometric frustration can also be seen from the finite-temperature LDFA calculations displayed in Fig. 5(a). There, the Néel temperatures are displayed as a function of interaction for different anisotropy strengths. Strictly speaking, there is no finite-temperature magnetic transition in two dimensions, according to the Mermin-Wagner theorem[50]. The transition still appears in a method that includes certain implicit IR cutoffs, such as that given by the partial mean-field character in DMFT and LDFA. The numerical finding is useful anyway, as the magnetic correlations are correctly described in this type of calculations. Furthermore, the finite-temperature magnetically ordered phase can be realized in a slab of multilayer triangular systems, where the mean field character of DMFT and LDFA can mimic the generic effect of three-dimentional coupling. In our study, the Néel temperatures are obtained from the extrapolation of the inverse spin susceptibility. Following Eq. (10), we calculate $\chi^s_Q(i\Omega_m = 0)$ in the entire first Brillouin zone (BZ) and extrapolate the inverse of the leading value of the temperature-dependent $\chi_Q(i\Omega_m = 0)$ to $T/t = 0$. The Néel temperature is given by the temperature where the extrapolated $\chi^{-1}_Q(i\Omega_m = 0)$ becomes zero. Examples of the spin susceptibilities and the extrapolation can be found, in Fig. 5(b) for $t'/t = 0.6$.

As shown in Fig. 5(a), increasing the anisotropy strength greatly suppresses the Néel temperature, especially in the weak-coupling region. At $t'/t = 0$, the square lattice is recovered and the Néel temperature is nonzero for any finite interaction ($U_c = 0$), indicating that long-range magnetic correlations are well established for $U/t > 0$. Increasing t'/t results in the suppression of the Néel temperature; as a result U_c increases. This coincides with what is obtained from the $T = 0$ VCA calculations shown in Fig. 3. Still, we cannot expect an exact quantitative agreement on U_c from these two methods, because both of them are subject to certain approximations. On the current level of approximation (see Sec. II for more details about the reference system size and the self-energy diagrams considered), Figs. 5(a) and 3 converge to the same conclusion, that the enhanced spatial anisotropy stabilizes an extended metallic phase and suppresses the propensity to magnetic ordering.

When the system approaches the antiferromagnetic state as a function of U or T, the magnetic correlations drive the spin susceptibility divergently but also leave fingerprints in the single-particle spectra. In the case of the square lattice, with the development of commensurate $Q = (\pi, \pi)$ antiferromagnetism, the effective magnetic unit cell becomes twice the size of the original unit cell. The single-particle spectra then pick up the new symmetry associated with the magnetic unit cell, which results in a "shadow band" around the Γ point[51]. In the fully isotropic triangular case, the magnetic correlation is of the 120° type. The resulting magnetic unit cell is then three times the size of the original unit cell. The original band will further be folded with respect to the magnetic zone boundary, which will also generate a shadow band around Γ. Thus, detecting the appearance of the shadow band can help us track the magnetic correlations of the system from the analysis of single-particle spectra.

Comparing DMFT and LDFA data is instructive to

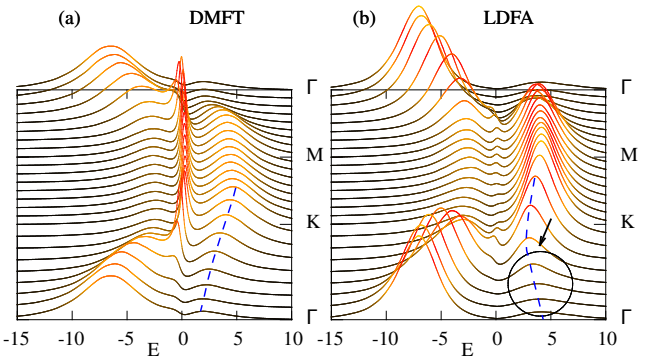

FIG. 6. Momentum dependence of the spectra for the triangular Hubbard model calculated from (a) DMFT and (b) LDFA with anisotropy strength $t'/t = 0.8$ at $T/t = 0.154$ and $U/t = 9.0$. Due to the development of antiferromagnetic correlations, a shadow band appears above the Fermi level around the Γ point, as shown in the circle in (b). The arrow indicates the symmetry shift induced by the appearance of the shadow band. This shadow band is absent in the DMFT calculation. The coherent peak at the Fermi energy $E = 0$ is not suppressed due to the missing of non-local correlations.

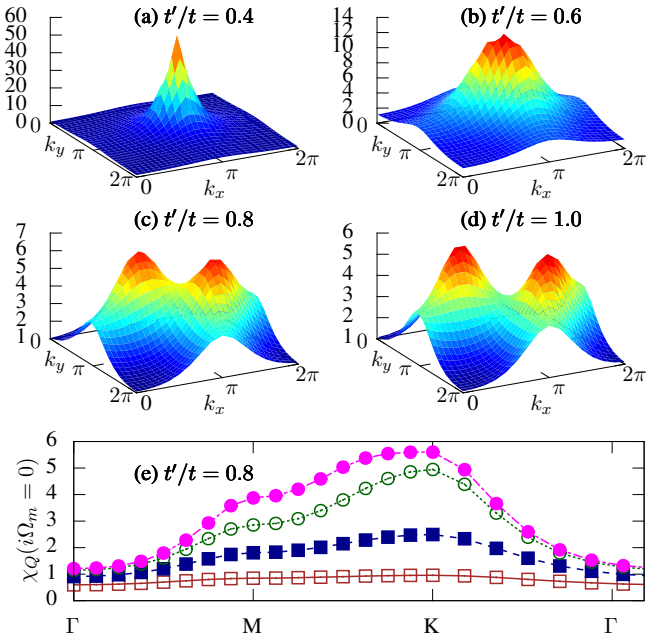

FIG. 7. (a)-(d) Spin susceptibilities $\chi_Q(i\Omega_m = 0)$ for $T/t \sim 0.286$ and $U/t = 9$ with different anisotropy strengths. The temperature is chosen to be low enough that all spin susceptibilities remain finite. The divergence of $\chi_Q(i\Omega_m = 0)$ indicates the development of magnetic order with the corresponding $\vec{Q}$. (e) Formation of the antiferromagnetic correlation with the decrease of temperature for $t'/t = 0.8$ and $U/t = 9$. From bottom to top, temperatures vary as $T = 1.0, 0.5, 0.33, 0.25$.

highlight the additional non-local corrections kept in LDFA. A detrimental problem of the DMFT lies in the local approximation, making it incapable of describing long-range correlations. Thus, the shadow band induced by the magnetic correlation should be less obvious or even absent in a DMFT calculation. In Fig. 6, we show the single-particle spectra for $t'/t = 0.8$, $U/t = 9$, and $T/t = 0.154$. The LDFA calculations were performed on the Matsubara axis, and the transformation to the real-frequency axis is accomplished by using the stochastic analytical continuation[52]. The chosen temperature is slightly above the Néel temperature, at which the magnetic correlations begin to fully unfold. We thus would expect new folded bands to appear in the single-particle spectra. In Fig. 6(b), as indicated in the circle, there is a band with less intensity that develops around Γ. This band is absent in the tight-binding model of Eq. (1) and is a direct result of the band backfolding with respect to the magnetic zone boundary. The symmetry shift induced by the enlarged magnetic unit cell is indicated by the arrow in Fig. 6(b). This shadow band locates at a finite energy at the Γ point, resulting in a slope change of the band above the Fermi level, as indicated by the blue dashed line in Fig. 6(b). This magnetic-ordering-induced shadow band is not correctly resolved in the DMFT calculation. As displayed in Fig. 6(a), the band close to Γ is not a band folded from the emergent symmetry, *i.e.*, the 120° symmetry; it is only the reminiscence of the band between M and K. It gradually approaches zero energy at the Γ point, as can be seen by following the blue dashed line. Another clear difference between the DMFT and the LDFA results lies in the suppression of the quasi-particle peak at the Fermi level. This is again due to the non-locality missing in the local approximation of the DMFT, which is accurately kept in LDFA.

The transition between the two types of magnetic order in Fig. 3 is also observed at finite temperature. Figure 7 shows the momentum-dependent susceptibilities $\chi_Q(i\Omega_m = 0)$ in the entire first BZ at $U/t = 9$ and $T/t \sim 0.286$, for four representative values of t'/t. As discussed in Sec. II, the instability of the paramagnetic solution reveals the formation of a magnetically ordered phase. As shown in Fig. 7(a) and Fig. 7(b), with smaller anisotropic strengths, $\chi_Q(i\Omega_m = 0)$ shows a single-peak located at the Néel-AFM $Q = (\pi, \pi)$. The increase of t'/t results in peak broadening as for the case of $t'/t = 0.6$ depicted in Fig. 7b. A further increase of the anisotropy strength splits the peak, and generates a double-peak structure of the spin susceptibility, which highlights the evolution from Néel-AFM to the 120°-AFM. At $t'/t = 1.0$, the valley between the two peaks at $(2\pi/3, 2\pi/3)$ and $(4\pi/3, 4\pi/3)$ becomes even deeper. It agrees with our VCA results (Fig. 3).

At finite temperatures, the LDFA allows us to analyze the thermodynamics of the Hubbard model on the anisotropic triangular lattice. In one of our recent works[53], by using LDFA, we showed that thermodynamical quantities such as the entropy substantially enhance our understanding of the competing roles of geometric frustration and electronic correlations. We found that

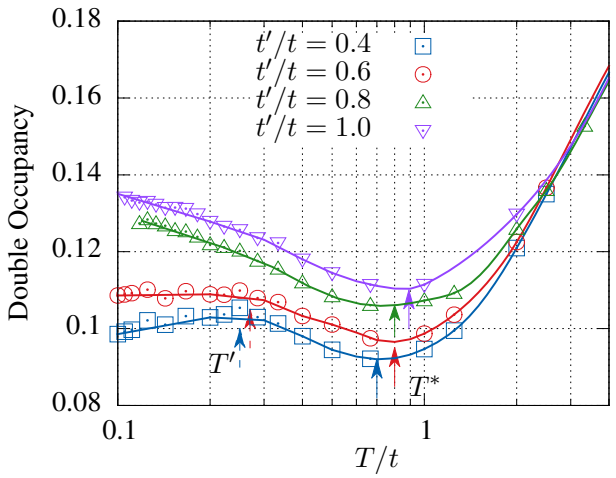

FIG. 8. The double occupancy D displays an individual temperature dependence for different anisotropy strengths. $U/t = 6$, and for all temperatures studied in LDFA, the system remains metallic for this interaction strength.

geometric frustration favors the effect of "adiabatic cooling"; that is, following a constant entropy curve, increasing the interaction results in an effective decrease in temperature. This is in contrast to the situation in square[54] and cubic[55] lattices, where the entropy is nearly a constant function of interaction in the weak-coupling region. The effect of "adiabatic cooling" has been found for the honeycomb-type lattice[56]. We speculate that the geometric frustration as imposed by the triangular lattice enhances the decrease in entropy as a function of interaction strength, which is discussed in the following.

Figure 8 displays the double occupancy $D = \langle n_\uparrow n_\downarrow \rangle$, whose low-temperature behavior reveals more information than just the degree of electron localization. The double occupancy relates to the entropy S through a Maxwell relation via the Hellmann-Feynman theorem, *i.e.*

$$(\frac{\partial S}{\partial U})_{T,V} = -(\frac{\partial D}{\partial T})_{U,V}. \tag{11}$$

As discussed in Ref. 53, the negative-entropy slope for temperatures lower than a characteristic temperature T^* indicates that the entropy will increase with the increase in interactions. As shown in Fig. 8, for temperatures smaller than $T^*/t \sim 0.8$, in the isotropic triangular case (*i.e.*, $t'/t = 1$), D decreases upon increasing T[53]. It becomes more intuitive by rewriting Eq. (11) as

$$\frac{C_v}{T}\left(\frac{\partial T}{\partial U}\right)_S = \left(\frac{\partial D}{\partial T}\right)_U, \tag{12}$$

where C_v is the specific heat. This immediately implies that, keeping the entropy constant, an increase in U results in a decrease in T for $T \leq T^*$. The influence of frustration effects becomes clear in Fig. 8. With the reduction in anisotropy, the negative slope of the double occupancy below T^* becomes less obvious. In the unfrustrated limit, *i.e.*, $t'/t = 0$, the double occupancy would resemble that in a square lattice, indicating that no "adiabatic cooling" is possible. At a fixed temperature below T^*, frustration increases the value of the double occupancy, resulting in the enhancement of its negative slope. We conclude that frustration is the reason for the "adiabatic cooling" in the anisotropic triangular system. In addition to the change of the slope, we find that the characteristic temperature T^* becomes slightly smaller with the decrease of t'/t (see the solid arrows around $T/t \sim 0.8$ in Fig. 8). In the curves for $t'/t = 0.4, 0.6$, we also observe a second characteristic temperature T' due to the evolution of system geometry from square to triangular (dashed arrows around $T/t \sim 0.25$).

IV. CONCLUSIONS

We have conducted a detailed single-particle spectral analysis of the Hubbard model on the anisotropic triangular lattice for zero and finite temperatures. Focusing on the role of anisotropy and interaction strength, we have identified the significant features of the phase diagram displaying, e.g., a magnetic transition regime between Néel-AFM and 120°-AFM orders as well as, in particular, a non-magnetic insulating regime. Once set at an anisotropy value near the triangular limit, the NMI domain quickly broadens in terms of the range of U/t as a function of anisotropy, along with a more extended metallic regime for weaker coupling. It is exactly the NMI regime which might prove the most relevant for unconventional organic compounds, as one or several spin-liquid phases can potentially appear in this window of parameter space. While this question is beyond the framework of the current investigation, which focused on single-particle quantities, it will be worthwhile to follow up on the identification of the NMI regime and to adapt methods capable of calculating multiparticle vertices in order to identify the nature of the quantum many-body phase. Along this path, our VCA/LDFA study is helpful in that it constrains the interesting parameter window to be scanned by other approaches such as variational Monte Carlo methods. At finite temperature, in line with our $T = 0$ study, we find that the anisotropy substantially suppresses the magnetic ordering of the system. The formation of the shadow band at the Γ point in the LDFA calculations shows that, going beyond DMFT, the LDFA is capable of describing magnetic effects due to the inclusion of non-local correlations. A characteristic temperature T^* is identified in the double occupancy, below which the double occupancy decreases upon increasing temperature. This opens up the possibility of "adiabatically cooling" the system by increasing the interactions while keeping the entropy constant. We find that the geometrical anisotropy favors "adiabatic cooling", that is, increasing the anisotropy results in a larger negative slope of the double occupancy below T^*.

Note added. Recently, we became aware of a related VCA study of the anisotropic triangular Hubbard model by Yamada[57]. The subset of VCA findings contained in our paper agrees with this study.

V. ACKNOWLEDGEMENT

W.H. and R.T. acknowledge the hospitality of the KITP where some of this work was finished and supported by the workshop program NSF PHY11-25915. G.L., M.L. and W.H. acknowledge the DPG Grant Unit FOR1162. R.T. and W.H. are supported by the European Research Commission through ERC-StG-TOPOLECTRICS-336012. We thank LRZ Munich for generous allocation of CPU time.

Appendix A: Technical refinements and caveats of the VCA

In this appendix, we present useful technical improvements to the VCA method for the current study. They concern the efficient simulation of more nonlocal fluctuations in a small reference cluster, and the precise determination of the spectral function from the pole structures of the single-particle Green's function. Furthermore, we illustrate the importance of an appropriate choice of reference cluster. Specifically, we show that the analysis of superconductivity is heavily affected by the discrete rotation symmetries of the reference cluster, rendering the VCA approach inaccurate for a reliable investigation of superconductivity for the anisotropic triangular lattice.

1. Variation of single-particle hopping

The variation of single-particle hopping t in VCA is usually not important for the study of strongly correlated systems, as its influence is negligibly small. We recently found, however, that this effect becomes important for the Hubbard model on the honeycomb lattice with small and intermediate correlations[28], which is also in line with previous studies on the square lattice[22,58]. In the current study, this is the regime where the MIT happens, and the NMI phase emerges in proximity to a metallic domain. Thus, we find that the variation of the single-particle hopping t is crucial for the analysis of the Hubbard model on the anisotropic triangular lattice.

Figure 9 displays the grand potential as a function of $\delta t = t' - t$, where t' is the optimal value of t that minimizes the grand potential. At $U/t = 7.0$, the minimum of the grand potential is at $\delta t/t \sim 1$, representing a strong enhancement of the dynamics within the reference cluster, as $t' \sim 2t$. The adjusted dynamics leads to an increase in the critical value for the MIT to $U/t \sim 7.5$. The minima of the grand potential move to $\delta t/t = 0.10$ and 0.08 as interactions increase to $U/t = 7.6$ and $U/t = 7.8$, respectively. Figure 9 clearly shows the trend of $\delta t \to 0$ when stronger interactions are present. In contrast to the MIT, the magnetic phase transition of the Hubbard model on the isotropic triangular lattice takes place at even stronger interactions $U/t = 9.4$, where the variation of the hopping is found to be negligible. As a consequence, with the variation of the single-particle hopping t, the NMI phase appears to be in the regime $7.5 < U/t < 9.4$, which nicely agrees with other works, some of which employ different approaches[42–48].

2. Exact evaluation of the single-particle gap through spectra function without broadening factor

In VCA, the spectral function as well as the local density of states (LDOS) is usually calculated from the single-particle Green's function with an broadening factor $i\eta$. A precise value of the single-particle gap can be only obtained by extrapolating η to zero. Here, we present a scheme to evaluate the exact single-particle gap without any such broadening factor η. The single-particle Green's function is calculated[59] as

$$G = \frac{1}{(QgQ^\dagger)^{-1} - V} = Q\frac{1}{g^{-1} - Q^\dagger V Q}Q^\dagger\,, \qquad \text{(A1)}$$

where $g^{-1} = \omega - \Lambda$ is a diagonal matrix and $\Lambda_{mn} = \delta_{mn}\omega'_m$ is the excitation spectrum of the reference cluster. The poles of the VCA Green's function G are simply the eigenvalues of the matrix $M = \Lambda + Q^\dagger V Q$. With the diagonal form of M, *i.e.*, $D_M = S^{-1}MS$, one can rewrite

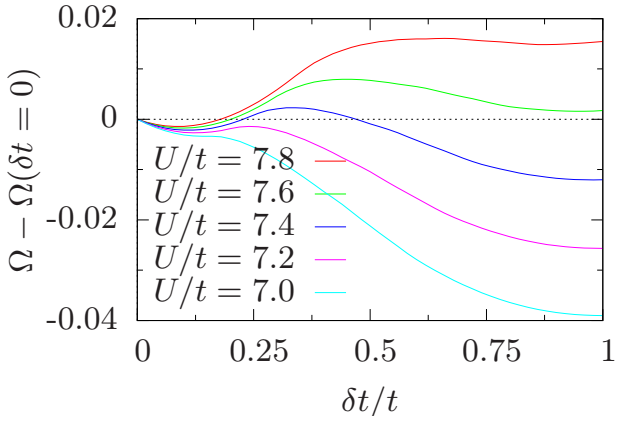

FIG. 9. VCA grand potential as a function of $\delta t/t$. In the metallic phase, *i.e.*, $U/t < 7.5$, the minimum is around $\delta t/t \sim 1$, representing a strong non-local modification of the hopping amplitude inside the reference cluster. This is not seen for the insulating regime where $U/t > 7.5$, as the minimum of $\delta t/t$ quickly moves to zero. For the two specific values of U/t shown in this plot, the minima are at $\delta t/t = 0.1$ for $U/t = 7.6$ and at $\delta t/t = 0.08$ for $U/t = 7.8$. The correction implied by the variation of t becomes negligible in the strongly correlated regime.

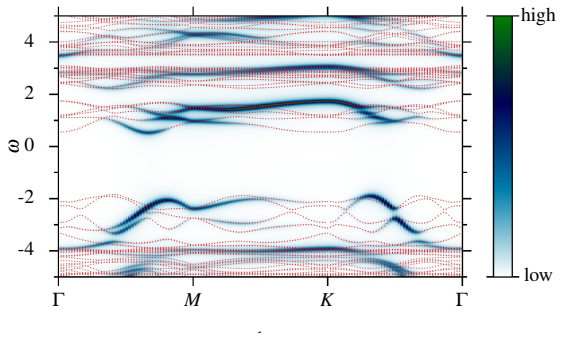

FIG. 10. Comparison of the spectral function calculated with a phenomenological broadening $\eta = 0.1$ (density plot with color code) and the exact pole structure of the Green's function with non-zero weight (red dots).

the VCA Green's function as

$$G = Q\frac{1}{M}Q^\dagger = Q\frac{1}{SD_MS^\dagger}Q^\dagger = QS\frac{1}{D_M}S^\dagger Q^\dagger\,. \quad \text{(A2)}$$

The weights associated with the poles D_M are $(QS)_{\alpha m}(S^\dagger Q^\dagger)_{m\beta}$. Only poles with nonzero weights contribute to the spectral function. In Fig. 10 we compare the spectra calculated from Eq. (A2) to the ones calculated after introducing a broadening factor. Clearly, the employment of Eq. (A2) gives rise to much richer spectra, where some parts in the intensity plot are missing for the calculations with broadening. This new strategy enhances the accuracy of the VCA method in characterizing the MIT through the single-particle gap as shown in Fig. 4(a).

3. Artificial bias for superconductivity from broken symmetries in VCA reference clusters

In the VCA phase diagram Fig. 3, no superconductivity (SC) was investigated. In principle, it is possible in VCA to study SC via appropriate Weiss fields, and indeed, this has been previously attempted for the Hubbard model on the anisotropic triangular lattice[30]. In the following, we show that these previous approaches have to be interpreted with extreme caution, and explicate why a systematic investigation of SC order for the anisotropic triangular lattice is not feasible for VCA or any other finite cluster method as a matter of principle. Figure 3 shall thus be understood as a tentative phase diagram without the inclusion of SC. For the isotropic triangular lattice where SC can be investigated reliably through VCA, we find chiral d-wave SC for a large window from weak to intermediate coupling, a superconducting solution which was not considered in Ref. 30.

Figure 11 shows the symmetry classification for the small-size reference clusters we encounter for the anisotropic triangular lattice. As we intend to interpolate

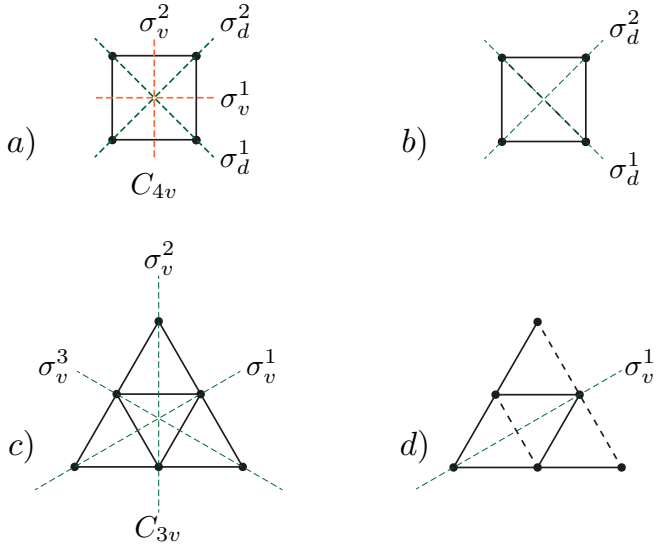

FIG. 11. Cluster symmetries. a) Four-site with square-lattice C_{4v} symmetry. b) Anisotropic four-site cluster cluster. c) Six-site with triangular-lattice C_{3v} symmetry. (d) Anisotropic six-site cluster.

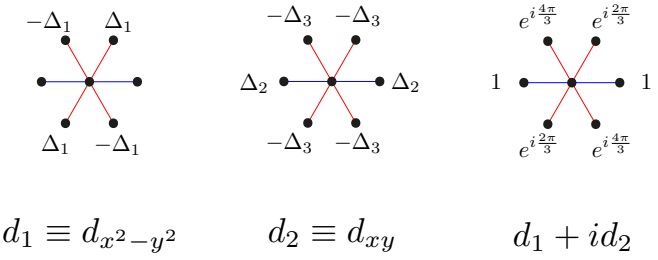

FIG. 12. Real-space superconducting form factors for the anisotropic triangular lattice. The amplitude parameters δ_i, $i = 1, 2, 3$, are varied in the VCA grand potential. d_1 and d_2 parametrize the SC orders, which become (left) $d_{x^2-y^2}$ and (middle) d_{xy} SC order in the isotropic square and triangular limits, respectively. (right) For the isotropic triangular lattice, in units of Δ_2, we find chiral d-wave SC order $d_1 + id_2 = d_{x^2-y^2} + id_{xy}$ for $\Delta_1 = \sqrt{3}/2$ and $\Delta_3 = 1/2$.

between the square lattice ($t'/t = 0$) and the triangular lattice ($t'/t = 1$), we choose a six-site cluster which is still conveniently tractable numerically and exhibits commensurability with C_{4v} and C_{3v} in the respective limits. (As further elaborated on in the main text, this also applies to the 12-site cluster which we, due to the significantly greater numerical effort used only for special points in the phase diagram.)

In close analogy to magnetic order, SC Weiss fields can be similarly employed in VCA. The relevant SC form factors are the in-plane d-wave orders $d_{x^2-y^2}$ (Fig. 12, left) and d_{xy} (Fig. 12, middle), which in total yield three variational SC amplitude parameters Δ_i, $i = 1, 2, 3$. For C_{4v}

symmetry ($t'/t = 0$), both d-wave orders are associated with independent one-dimensional irreducible lattice representations. For C_{3v} symmetry ($t'/t = 1$), they form a single two-dimensional irreducible lattice representation. For generic t'/t, the SC orders are denoted by d_1 and d_2, respectively.

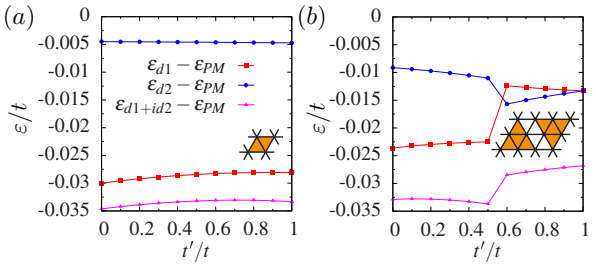

FIG. 13. Condensation energy of the (a) four-site and (b) six-site cluster ground state for different SC order parameters relative to the paramagnetic ground state $\varepsilon_{d_i} - \varepsilon_{PM}$. All energies are taken at $U/t = 5$ with fixed respectively chosen SC Weiss field $h = 0.1t$. $d_1 + id_2$ maximizes the condensation energy for finite clusters as it removes all low-energy spectral weight.

Let us first analyze the finite-cluster spectra in the presence of the SC Weiss fields. In Fig. 13, the energy differences between the paramagnetic ground state and the SC ground state are plotted as a function of anisotropy for the four-site and six-site clusters and $U/t = 5$. The Weiss field scale h/t=0.1 is big enough that the complex chiral d-wave order parameter $d_1 + id_2$ (Fig. 12, right) is energetically preferred. This relates to the fact that only $d_1 + id_2$ is fully gapped, while both individual d_1 and d_2 retain nodal behavior. (Note, however, this does not mean that chiral superconductivity should always be preferred for the infinite VCA system where $h \to 0$ or for a finite-cluster spectrum with smaller h/t.)

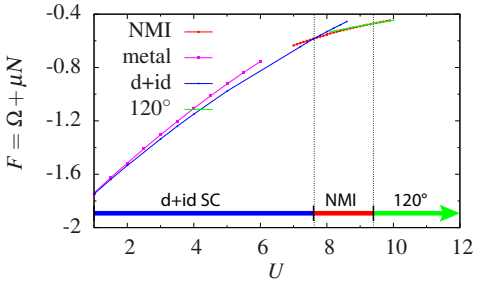

FIG. 14. VCA free energy of the Hubbard model on the isotropic triangular lattice for a six-site reference cluster. $d + id$ SC is stabilized in the weak- to intermediate-coupling regime. It only partly overlays the NMI phase obtained in Fig. 3.

Figure 13(a) shows the four-site cluster spectrum, which hardly changes as a function of anisotropy. Of the individual d-wave form factors, $d_1 \equiv d_{x^2-y^2}$ has the larger condensation energy for any anisotropy. This changes as one considers the six-site cluster [Fig. 13(b)]. Beyond a certain degree of anisotropy towards the triangular limit, d_2 is preferred over d_1. Eventually, d_1 and d_2 become degenerate for $t'/t = 1$, as dictated by C_{3v} lattice symmetry. Figure 13 demonstrates how the fundamental symmetries of the isotropic triangular limits are violated by the four-site cluster, as, e.g., employed in Ref. 30. Taking the six-site cluster and hence accurately accounting for lattice symmetries, the VCA phase diagram for the isotropic triangular lattice is shown in Fig. 14. From weak to intermediate coupling, chiral d-wave SC is found, followed by an NMI regime and 120°-AFM order for increasing U/t. The nature of superconductivity found in our VCA analysis is in accordance with several approaches such as the functional renormalization group[60–62], parquet renormalization group[63], and finite-cluster variational Monte Carlo[64]. Note in Fig. 14 that the NMI phase, as the promising spin-liquid candidate scenario, persists upon the joint consideration of SC for a sizable coupling regime.

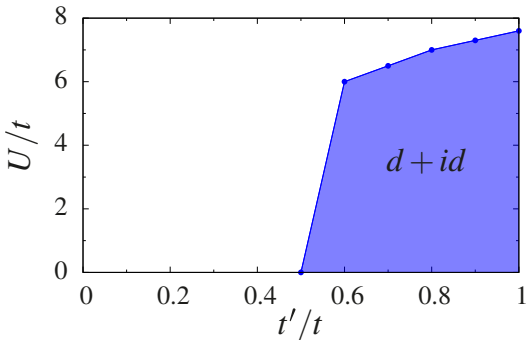

FIG. 15. Domain of stable $d + id$ SC grand potential saddle point in VCA for the anisotropic six-site reference cluster.

How does the SC phase diagram in Fig. 14 evolve for finite anisotropy $t'/t < 1$ when d_1 and d_2 are no longer degenerate? $d_1 + id_2$ dominates as long as the enhanced gain of the condensation energy through chiral d-wave SC overcomes the energy splitting between d_1 and d_2. (Figure 15 shows the domain for which a saddle point of chiral d-wave SC is found in VCA with a six-site reference cluster.) Overall, however, the bias from different cluster sizes, as well as strong finite-size effects in the small clusters in general, does not allow for a systematic analysis of SC for the anisotropic lattice. For example, the quantitative analysis of the transition point between the gaped chiral d wave and nodal d wave does not appear feasible within VCA: The four-site analysis yields a strong preference for $d_{x^2-y^2}$-wave SC, while the six-site analysis advocates the chiral d wave for a large domain of anisotropy. Overall, our findings support the view that such a question should preferably be addressed through momentum-resolved approaches in which the adjusted breaking of lattice symmetries is more accurately accounted for than in a finite-size real-space cluster method.

[1] S. Lefebvre, P. Wzietek, S. Brown, C. Bourbonnais, D. Jérome, C. Mézière, M. Fourmigué, and P. Batail, Phys. Rev. Lett. **85**, 5420 (2000).
[2] Y. Kurosaki, Y. Shimizu, K. Miyagawa, K. Kanoda, and G. Saito, Phys. Rev. Lett. **95**, 177001 (2005).
[3] F. Kagawa, K. Miyagawa, and K. Kanoda, Nature **436**, 534 (2005).
[4] Y. Shimizu, K. Miyagawa, K. Kanoda, M. Maesato, and G. Saito, Phys. Rev. Lett. **91**, 107001 (2003).
[5] W. Zheng, R. R. P. Singh, R. H. McKenzie, and R. Coldea, Phys. Rev. B **71**, 134422 (2005).
[6] C. P. Nave and P. A. Lee, Phys. Rev. B **76**, 235124 (2007).
[7] Y. Qi, C. Xu, and S. Sachdev, Phys. Rev. Lett. **102**, 176401 (2009).
[8] C. Xu and S. Sachdev, Phys. Rev. B **79**, 064405 (2009).
[9] S.-S. Lee and P. A. Lee, Phys. Rev. Lett. **95**, 036403 (2005).
[10] M. Barkeshli, H. Yao, and S. A. Kivelson, Phys. Rev. B **87**, 140402 (2013).
[11] S. Yamashita, Y. Nakazawa, M. Oguni, Y. Oshima, H. Nojiri, Y. Shimizu, K. Miygawa, and K. Kanoda, Nature Phys. **4**, 459 (2008).
[12] M. Yamashita, N. Nakata, Y. Kasahara, T. Sasaki, N. Yoneyama, N. Kobayashi, S. Fujimoto, T. Shibauchi, and Y. Matsuda, Nature Phys. **5**, 44 (2009).
[13] K. Kanoda and R. Kato, Annual Review of Condensed Matter Physics **2**, 167 (2011).
[14] B. J. Powell and R. H. McKenzie, Reports on Progress in Physics **74**, 056501 (2011).
[15] H. C. Kandpal, I. Opahle, Y.-Z. Zhang, H. O. Jeschke, and R. Valentí, Phys. Rev. Lett. **103**, 067004 (2009).
[16] K. Nakamura, Y. Yoshimoto, T. Kosugi, R. Arita, and M. Imada, Journal of the Physical Society of Japan **78**, 083710 (2009).
[17] K. Nakamura, Y. Yoshimoto, and M. Imada, ArXiv e-prints (2012), arXiv:1208.3954 [cond-mat.str-el].
[18] J. Reuther and R. Thomale, Phys. Rev. B **83**, 024402 (2011).
[19] M. Potthoff, M. Aichhorn, and C. Dahnken, Phys. Rev. Lett. **91**, 206402 (2003).
[20] M. Potthoff, The European Physical Journal B - Condensed Matter and Complex Systems **32**, 429 (2003).
[21] M. Potthoff, Adv. Solid State Phys. **45**, 135 (2005).
[22] C. Dahnken, M. Aichhorn, W. Hanke, E. Arrigoni, and M. Potthoff, Physical Review B **70**, 245110 (2004).
[23] D. Sénéchal, P.-L. Lavertu, M.-A. Marois, and A.-M. S. Tremblay, Phys. Rev. Lett. **94**, 156404 (2005).
[24] M. Aichhorn and E. Arrigoni, EPL (Europhysics Letters) **72**, 117 (2005).
[25] W. Hanke, M. Kiesel, M. Aichhorn, S. Brehm, and E. Arrigoni, The European Physical Journal Special Topics **188**, 15 (2010).
[26] S. Brehm, E. Arrigoni, M. Aichhorn, and W. Hanke, EPL (Europhysics Letters) **89**, 27005 (2010).
[27] S.-L. Yu, X. C. Xie, and J.-X. Li, Phys. Rev. Lett. **107**, 010401 (2011).
[28] M. Laubach, J. Reuther, R. Thomale, and S. Rachel, Phys. Rev. B **90**, 165136 (2014).
[29] G. Li, M. Laubach, A. Fleszar, and W. Hanke, Phys. Rev. B(R) **83**, 041104 (2011).
[30] P. Sahebsara and D. Sénéchal, Phys. Rev. Lett. **97**, 257004 (2006).
[31] P. Sahebsara and D. Senechal, Phys. Rev. Lett. **100**, 136402 (2008).
[32] A. N. Rubtsov, M. I. Katsnelson, A. I. Lichtenstein, and A. Georges, Phys. Rev. B **79**, 045133 (2009).
[33] H. Hafermann, G. Li, A. N. Rubtsov, M. I. Katsnelson, A. I. Lichtenstein, and H. Monien, Phys. Rev. Lett. **102**, 206401 (2009).
[34] A. Georges, G. Kotliar, W. Krauth, and M. J. Rozenberg, Rev. Mod. Phys. **68**, 13 (1996).
[35] A. N. Rubtsov, V. V. Savkin, and A. I. Lichtenstein, Phys. Rev. B **72**, 035122 (2005).
[36] G. Li, H. Lee, and H. Monien, Phys. Rev. B **78**, 195105 (2008).
[37] E. Manousakis, Rev. Mod. Phys. **63**, 1 (1991).
[38] B. Bernu, P. Lecheminant, C. Lhuillier, and L. Pierre, Phys. Rev. B **50**, 10048 (1994).
[39] L. Capriotti, A. E. Trumper, and S. Sorella, Phys. Rev. Lett. **82**, 3899 (1999).
[40] S. R. White and A. L. Chernyshev, Phys. Rev. Lett. **99**, 127004 (2007).
[41] B. Kyung and A.-M. S. Tremblay, Phys. Rev. Lett. **97**, 046402 (2006).
[42] H.-Y. Yang, A. M. Läuchli, F. Mila, and K. P. Schmidt, Phys. Rev. Lett. **105**, 267204 (2010).
[43] B. Kyung, Phys. Rev. B **75**, 033102 (2007).
[44] T. Watanabe, H. Yokoyama, Y. Tanaka, and J. ichiro Inoue, J. Phys. Soc. Jpn. **75,**, 074707 (2006), cond-mat/0602098.
[45] T. Watanabe, H. Yokoyama, Y. Tanaka, and J. Inoue, Phys. Rev. B **77**, 214505 (2008).
[46] L. F. Tocchio, H. Feldner, F. Becca, R. Valentí, and C. Gros, Phys. Rev. B **87**, 035143 (2013).
[47] S. Dayal, R. T. Clay, and S. Mazumdar, Phys. Rev. B **85,**, 165141 (2012), 1201.5139.
[48] T. Yoshioka, A. Koga, and N. Kawakami, Physical Review Letters **103**, 036401 (2009).
[49] J. Kuneš, Phys. Rev. B **83**, 085102 (2011).
[50] N. D. Mermin and H. Wagner, Phys. Rev. Lett. **17**, 1133 (1966).
[51] J. R. Schrieffer, X. G. Wen, and S. C. Zhang, Phys. Rev. B **39**, 11663 (1989).
[52] K. Beach, "Identifying the maximum entropy method as a special limit of stochastic analytic continuation," (2004), arXiv:cond-mat/0403055.
[53] G. Li, A. E. Antipov, A. N. Rubtsov, S. Kirchner, and W. Hanke, Phys. Rev. B **89**, 161118 (2014).
[54] T. Paiva, R. Scalettar, M. Randeria, and N. Trivedi, Phys. Rev. Lett. **104**, 066406 (2010).
[55] T. Paiva, Y. L. Loh, M. Randeria, R. T. Scalettar, and N. Trivedi, Phys. Rev. Lett. **107**, 086401 (2011).
[56] B. Tang, T. Paiva, E. Khatami, and M. Rigol, Phys. Rev. Lett. **109**, 205301 (2012).
[57] A. Yamada, Phys. Rev. B **89**, 195108 (2014).
[58] M. Aichhorn, H. G. Evertz, W. von der Linden, and M. Potthoff, Phys. Rev. B **70**, 235107 (2004).
[59] M. Aichhorn, E. Arrigoni, M. Potthoff, and W. Hanke, Physical Review B (Condensed Matter and Materials Physics) **74**, 235117 (2006).
[60] C. Honerkamp, Phys. Rev. B **68**, 104510 (2003).
[61] M. L. Kiesel, C. Platt, W. Hanke, and R. Thomale, Phys. Rev. Lett. **111**, 097001 (2013).

[62] C. Platt, W. Hanke, and R. Thomale, Adv. Phys. **62**, 453 (2013).
[63] R. Nandkishore, R. Thomale, and A. V. Chubukov, Phys. Rev. B **89**, 144501 (2014).
[64] K. S. Chen, Z. Y. Meng, U. Yu, S. Yang, M. Jarrell, and J. Moreno, Phys. Rev. B **88**, 041103 (2013).